

Marginally compact fractal trees with semiflexibilityMaxim Dolgushev,^{1,2,*} Adrian L. Hauber,¹ Philipp Pelagejcev,¹ and Joachim P. Wittmer²¹*Institute of Physics, University of Freiburg, Hermann-Herder-Strasse 3, D-79104 Freiburg, Germany*²*Institut Charles Sadron, Université de Strasbourg & CNRS, 23 rue du Loess, 67034 Strasbourg Cedex, France*

(Received 7 June 2017; published 17 July 2017)

We study marginally compact macromolecular trees that are created by means of two different fractal generators. In doing so, we assume Gaussian statistics for the vectors connecting nodes of the trees. Moreover, we introduce bond-bond correlations that make the trees locally semiflexible. The symmetry of the structures allows an iterative construction of full sets of eigenmodes (notwithstanding the additional interactions that are present due to semiflexibility constraints), enabling us to get physical insights about the trees' behavior and to consider larger structures. Due to the local stiffness, the self-contact density gets drastically reduced.

DOI: [10.1103/PhysRevE.96.012501](https://doi.org/10.1103/PhysRevE.96.012501)**I. INTRODUCTION**

In nature, many objects can be successfully represented through fractal models [1–12]. Examples include lungs [2–4], plants [5], proteins [6,7], and chromatin [8–12], to name only a few. In addition, human-made materials, such as super-repellent surfaces [13,14], porous cements [15], super-lenses [16], and supercapacitors [17,18], can be build in a fractal way in order to make a better performance. The purpose of many of these examples requests an effective usage of the space provided for them. This challenge is usually connected to a very dense packing of the objects [8,19] and at the same time to a huge surface needed for their function (e.g., surface available for charge in case of supercapacitors [18]). Thus, in the best case almost all their constituents build a surface, e.g., for compact objects in three-dimensional space consisting of N units and having size $R \sim N^{1/3}$, the surface A scales as $A \sim R^3 \sim N$ [20].

With respect to the biological and technological examples listed above, it is worth mentioning another actively studied system—the melt of nonconcatenated and unknotted ring polymers [21–33]—that have been surmised to be marginally compact [25,28,31]. However, the marginal compactness of ring melts is controversially argued, partly due to the clever theoretical argument [23] that the marginal compactness leads to a logarithmic divergence of the self-contact density. In a recent work [20] by some of us, a practical way out of this difficulty was suggested. There we have studied the fractal trees of Ref. [34] (see tree \mathcal{T}_1 of Fig. 1) that are by construction marginally compact. These toy structures, not aiming to describe the full complexity of examples such as given by Refs. [2–18,21–33], allowed us to show that a simple ingredient that can suppress the divergent behavior of the self-contact density ρ_c is the linear spacers between branching points of the trees.

The present study focuses on another aspect of marginally compact trees, namely on the role of local semiflexibility. Recent studies [20,34] have considered Gaussian, marginally compact trees with interactions between topologically nearest-neighboring beads, i.e., in the framework of a generalized Rouse model [35]. In particular, this assumption implies that

the orientations of bonds are uncorrelated [35,36]. However, the price one has to pay for the bond correlations is a more complex structure of the dynamical matrix that then in the easiest case (under freely rotating bonds assumption for the nonadjacent bonds [37]) contains also the elements related to the next-nearest-neighboring beads [39]. Notwithstanding this difficulty, the framework of semiflexible treelike polymers (STP) of Ref. [39], where the semiflexibility is introduced at all beads (also at branching nodes), turned out to be very helpful in studying the relaxation dynamics of semiflexible dendrimers [40,41] and fractals [42,43]. Moreover, inclusion of bond-bond correlations has been shown to have a fundamental importance for NMR relaxation of dendrimers [44–47]. Therefore, the semiflexibility should also be an important ingredient for marginally compact trees.

In this work we consider marginally compact trees which are locally semiflexible. The topology of the trees is sketched in Fig. 1. Fractal tree \mathcal{T}_1 consists of beads of functionality 1, 2, and 3; the generalized Rouse [35] behavior (i.e., in the absence of bond-bond correlations) of these trees has been studied in Refs. [20,34]. In order to make our results more rigorous and to exemplify the role of functionality of branching nodes, we introduce another fractal generator that builds marginally compact trees \mathcal{T}_2 (see Fig. 1), which do not have any linear spacers but contain beads of functionality 4. Both trees \mathcal{T}_1 and \mathcal{T}_2 show all relevant scalings of marginally compact, flexible trees [20,34], when one introduces local bending rigidity. At the same time, the semiflexibility leads to a swelling of the structures and hence to an increase of the higher relaxation times and to a significant suppression of self-contacts. Yet the underlying STP framework [39] allows us to perform a detailed analysis of eigenmodes and to reduce the computational work.

The paper is structured as follows. In the next section, we provide theoretical formulas and details for the dynamical matrix in the STP framework [39], whose spectra for trees \mathcal{T}_1 and \mathcal{T}_2 are analyzed in Sec. III (the technical details are relegated to the Appendix). The static and dynamical properties of the trees are presented in Sec. IV. Section V closes the paper with a summary and conclusions.

II. THEORETICAL MODEL

We start this section with a brief recall of the theory of STP [39]. The STP framework allows to introduce local

*dolgushev@physik.uni-freiburg.de

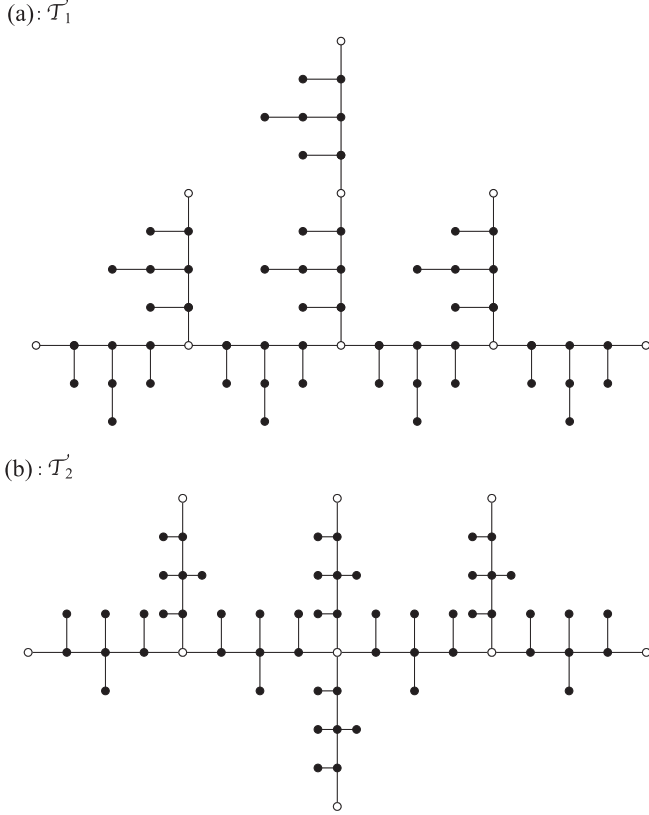


FIG. 1. Fractal trees \mathcal{T}_1 (a) and \mathcal{T}_2 (b) studied in this work. Both structures are at iteration $I = 2$. Beads shown as open circles represent the trees of initial iteration $I = 1$. The sketch is aimed only to present the topology of the fractal trees; their spatial conformations may appear in vastly different forms.

bending rigidity for Gaussian trees with arbitrary topology. The resulting dynamical matrix of the trees is sparse and has an analytically closed form.

In the STP theory the edges of the treelike structures represent Gaussian bonds $\{\mathbf{d}_i\}$, whose orientations are constrained. For any two adjacent bonds \mathbf{d}_i and \mathbf{d}_j one has $\langle \mathbf{d}_i \cdot \mathbf{d}_j \rangle = \pm b^2 q_m$, where $b^2 = \langle \mathbf{d}_i \cdot \mathbf{d}_i \rangle = \langle \mathbf{d}_j \cdot \mathbf{d}_j \rangle$ is the mean-square length of each bond and q_m is the so-called stiffness parameter related to bead m connecting bonds \mathbf{d}_i and \mathbf{d}_j . The sign determines connection of the bonds, plus sign corresponds to a head-to-tail connection and minus to two other configurations. The connection between nonadjacent bonds is taken in a freely rotating manner, i.e., for bonds connected through the path $\mathbf{d}_{k_1}, \dots, \mathbf{d}_{k_s}$ the relation $\langle \mathbf{d}_i \cdot \mathbf{d}_j \rangle = \langle \mathbf{d}_i \cdot \mathbf{d}_{k_1} \rangle \langle \mathbf{d}_{k_1} \cdot \mathbf{d}_{k_2} \rangle \dots \langle \mathbf{d}_{k_s} \cdot \mathbf{d}_j \rangle b^{-2s}$ holds [37].

Given that each bond \mathbf{d}_i has a zero mean, the average scalar products $\{\langle \mathbf{d}_i \cdot \mathbf{d}_j \rangle\}$ represent the covariance matrix $\Sigma = (\langle \mathbf{d}_i \cdot \mathbf{d}_j \rangle)$ that fully determines the Gaussian distribution of the bonds. Furthermore, each bond vector \mathbf{d}_i can be represented through a difference of position vectors of beads connected through \mathbf{d}_i , $\mathbf{d}_i = \mathbf{r}_n - \mathbf{r}_m$. With this, the potential energy of the tree,

$$V = \frac{3}{2} k_B T \sum_{i,j} (\Sigma^{-1})_{ij} \mathbf{d}_i \cdot \mathbf{d}_j = \frac{3k_B T}{2b^2} \sum_{m,n} A_{nm} \mathbf{r}_n \cdot \mathbf{r}_m, \quad (1)$$

is fully represented by the dynamical matrix $\mathbf{A} = (A_{nm})$. Based on the potential energy V , the dynamics of a polymer can be described by a set of Langevin equations, e.g., for the position of the k th bead one has

$$\zeta \frac{\partial}{\partial t} \mathbf{r}_k(t) + \frac{3k_B T}{b^2} \sum_n A_{kn} \mathbf{r}_n = \mathbf{g}_k(t), \quad (2)$$

where $\zeta \frac{\partial}{\partial t} \mathbf{r}_k(t)$ and $\mathbf{g}_k(t)$ are the friction and stochastic (white-noise) forces, respectively.

The conditions on the averaged scalar products used in the STP framework lead to an analytic form of \mathbf{A} . Moreover, under these conditions the matrix \mathbf{A} turns out to be very sparse. Its nonvanishing elements are either diagonal or related to nearest-neighboring and next-nearest-neighboring beads. For a bead of functionality f (i.e., it has f nearest neighbors) directly connected to beads of functionalities f_1, \dots, f_f , the diagonal element of \mathbf{A} reads

$$\mu_{f_1 \dots f_f}^{(f)} = \frac{f}{1 - (f-1)q_f} + \sum_{s=1}^f \frac{(f_s-1)q_{f_s}^2}{1 - (f_s-2)q_{f_s} - (f_s-1)q_{f_s}^2}. \quad (3)$$

For two directly connected beads of functionalities f_1 and f_2 one has

$$\nu_{f_1 f_2} = -\frac{1 - (f_1-1)(f_2-1)q_{f_1}q_{f_2}}{[1 - (f_1-1)q_{f_1}][1 - (f_2-1)q_{f_2}]} \quad (4)$$

and for two next-nearest-neighboring beads connected through a bead of functionality f the corresponding element of \mathbf{A} is

$$\rho_f = \frac{q_f}{1 - (f-2)q_f - (f-1)q_f^2}. \quad (5)$$

In Eqs. (3)–(5) the stiffness parameters q_{f_i} are related to the beads (junctions) of functionality f_i . Each stiffness parameter q_{f_i} is bounded from above by $1/(f_i-1)$ [39,48]; if all stiffness parameters are zero, then one recovers fully flexible structures so the dynamical matrix \mathbf{A} transforms into the connectivity (Laplacian) matrix.

We note that the STP theory allows us to choose the stiffness parameters at every junction separately. Here, however, a homogeneous case is used in which all junctions of the same functionality, say, $f \geq 2$, have the same stiffness parameter q_f . Moreover, here we assume a linear dependence of the stiffness parameters from each other by taking $q_f = q/(f-1)$ (with $f \geq 2$), so that the limits 0 and $1/(f-1)$ are reached simultaneously for all junctions by varying q from 0 to 1. For beads of functionality 1 no stiffness parameter can be assigned. This fact is automatically taken by Eqs. (3) and (4) into account, where the corresponding terms due to prefactors like (f_i-1) disappear.

Needless to say, the information about the behavior of STP in completely encoded in the eigenvalues and eigenvectors of the dynamical matrix \mathbf{A} . Moreover, the symmetry of the structures allows us to reduce computational efforts and to get physical insights of the relaxation behavior, as we proceed to show in Sec. III.

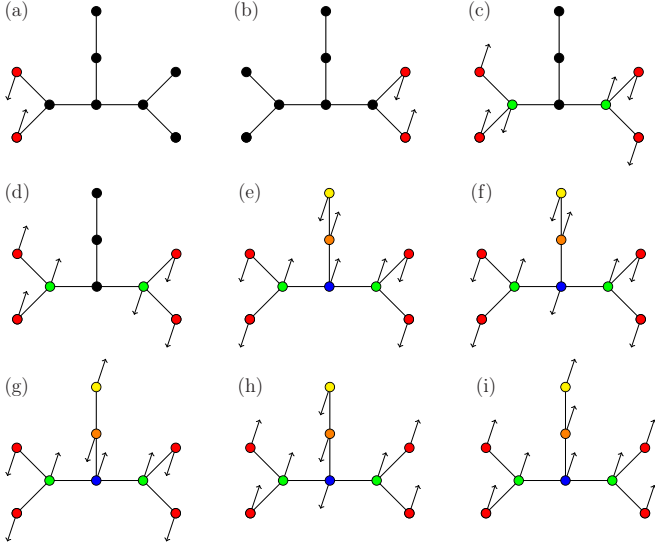


FIG. 2. Schematic sketch of eigenmodes of \mathcal{T}_1 for $I = 1$. Beads having the same amplitude are color coded. Black beads are immobile.

III. SPECTRUM OF THE DYNAMICAL MATRIX AND THE CORRESPONDING EIGENMODES

The symmetry of trees \mathcal{T}_1 and \mathcal{T}_2 allows an iterative construction of a full set of eigenvectors [49]. The construction procedure is rooted in the work of Cai and Chen [50] for flexible dendrimers, which has been extended to STP treatment of semiflexible dendrimers [40,41] and regular fractals [42,43].

We start with tree \mathcal{T}_1 at iteration $I = 1$. Figure 2 displays the eigenmodes of the structure. Those of Figs. 2(a)–2(d) leave some beads immobile, whereas in the eigenmodes of Figs. 2(e)–2(i) all beads are involved. The modes (a) and (b) represent two vectors, which contain only two nonzero entries $1/\sqrt{2}$ and $-1/\sqrt{2}$. The ensuing (double degenerate) eigenvalue is equal to $\mu_3^{(1)} - \rho_3$, i.e., the 1×1 matrix describing this motion

$$\mathbf{A}^{(1)}(\mathcal{T}_1) = [\mu_3^{(1)} - \rho_3]. \quad (6)$$

Next, we consider the modes displayed in Figs. 2(c) and 2(d) that have the shape $(x, x, \mp y, 0, 0, 0, \pm y, -x, -x)^T$. Multiplying the dynamical matrix with these vectors leads to a set of two nontrivial linear equations on x and y represented through the matrix

$$\tilde{\mathbf{A}}^{(1)}(\mathcal{T}_1) = \begin{bmatrix} \mu_3^{(1)} + \rho_3 & v_{13} \\ 2v_{13} & \mu_{113}^{(3)} - \rho_3 \end{bmatrix}. \quad (7)$$

Thus, diagonalization of $\tilde{\mathbf{A}}^{(1)}(\mathcal{T}_1)$ given by Eq. (7) leads to two eigenvalues of \mathbf{A} ; the smallest one is related to Fig. 2(d) and the other one to Fig. 2(c). The remaining five eigenvalues of \mathbf{A} are obtained from the diagonalization of the reduced matrix

$$\mathbf{B}^{(1)}(\mathcal{T}_1) = \begin{bmatrix} \mu_3^{(1)} + \rho_3 & v_{13} & 0 & 0 & \rho_3 \\ 2v_{13} & \mu_{113}^{(3)} + \rho_3 & 0 & \rho_3 & v_{33} \\ 0 & 0 & \mu_2^{(1)} & v_{12} & \rho_2 \\ 0 & 2\rho_3 & v_{12} & \mu_{13}^{(2)} & v_{23} \\ 4\rho_3 & 2v_{33} & \rho_2 & v_{23} & \mu_{233}^{(3)} \end{bmatrix}. \quad (8)$$

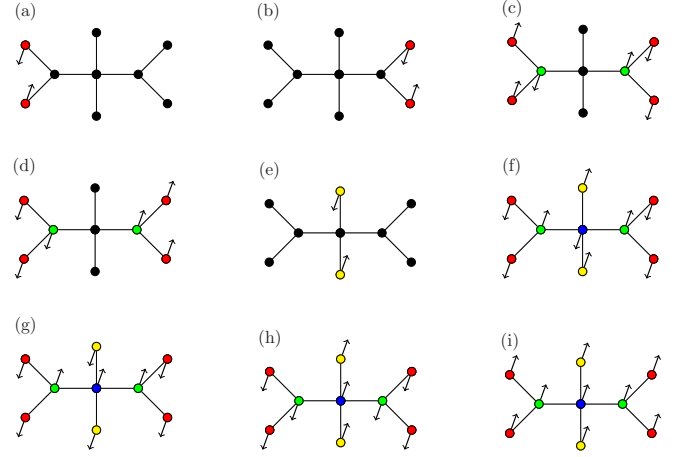


FIG. 3. Schematic sketch of eigenmodes of \mathcal{T}_2 for $I = 1$. Beads having the same amplitude are color coded. Black beads are immobile.

This matrix is related to the eigenmodes of Figs. 2(e)–2(i). For each of these modes the beads that are symmetric with respect to the core (blue bead) move in the same direction and with the same amplitude. Figure 2(i) depicts the translational mode $(1, \dots, 1)^T / \sqrt{N} = (1/3, \dots, 1/3)^T$ related to the eigenvalue $\lambda_0 = 0$.

The construction of eigenmodes for tree \mathcal{T}_2 goes in a similar manner, see Fig. 3. The modes of Figs. 3(a) and 3(b) are related to the reduced matrix

$$\mathbf{A}^{(1)}(\mathcal{T}_2) = [\mu_3^{(1)} - \rho_3] \quad (9)$$

that is equal to $\mathbf{A}^{(1)}(\mathcal{T}_1)$ of Eq. (6). The matrix $\tilde{\mathbf{A}}^{(1)}(\mathcal{T}_2)$ corresponding to Figs. 3(c) and 3(d) differs slightly from $\tilde{\mathbf{A}}^{(1)}(\mathcal{T}_1)$ of Eq. (7) due to the core bead of functionality 4,

$$\tilde{\mathbf{A}}^{(1)}(\mathcal{T}_2) = \begin{bmatrix} \mu_3^{(1)} + \rho_3 & v_{13} \\ 2v_{13} & \mu_{114}^{(3)} - \rho_4 \end{bmatrix}. \quad (10)$$

Differently from \mathcal{T}_1 , tree \mathcal{T}_2 has for $I = 1$ five eigenmodes that leave some beads (including the core) immobile. So the mode of Fig. 3(e) leads to the eigenvalue $\mu_4^{(1)} - \rho_4$, which can be formulated as 1×1 matrix,

$$\hat{\mathbf{A}}^{(1)}(\mathcal{T}_2) = [\mu_4^{(1)} - \rho_4]. \quad (11)$$

The remaining four eigenvalues related to Figs. 3(f)–3(i) come from the diagonalization of

$$\mathbf{B}^{(1)}(\mathcal{T}_2) = \begin{bmatrix} \mu_{1133}^{(4)} & 2v_{14} & 4\rho_3 & 2v_{34} \\ v_{14} & \mu_4^{(1)} + \rho_4 & 0 & 2\rho_4 \\ \rho_3 & 0 & \mu_3^{(1)} + \rho_3 & v_{13} \\ v_{34} & 2\rho_4 & 2v_{13} & \mu_{114}^{(3)} + \rho_4 \end{bmatrix}. \quad (12)$$

As for \mathcal{T}_1 , this matrix has one vanishing eigenvalue related to the translational mode of Fig. 3(i).

The above procedure of construction of the sets of eigenmodes can be extended for higher $I > 1$. The respective reduced matrices can be build iteratively, see Appendix. Here we discuss the sizes of the reduced matrices and the degeneracy of the corresponding eigenvalues.

As observed for $I = 1$, the modes (a) and (b) of Figs. 2 and 3 lead to a double degenerate eigenvalue $[\mu_3^{(1)} - \rho_3]$. Going to the next iteration each bond gets replaced through a tree of iteration $I = 1$ (see Fig. 1), hence each bead of functionality 1 at iteration $I = 1$ leads to a pattern as displayed in Fig. 2(a) at iteration $I = 2$. At iteration $I - 1$ trees \mathcal{T}_1 and \mathcal{T}_2 have $(3 \times 8^{I-1} + 11)/7$ and $(4 \times 8^{I-1} + 10)/7$ beads with functionality 1, respectively. Thus the degeneracy of eigenvalue $(\mu_3^{(1)} - \rho_3)$ at iteration I is $(3 \times 8^{I-1} + 11)/7$ for \mathcal{T}_1 and $(4 \times 8^{I-1} + 10)/7$ for \mathcal{T}_2 . For tree \mathcal{T}_2 each bond of the previous iteration will lead to the pattern of Fig. 3(e). Hence the degeneracy of eigenvalue $[\mu_4^{(1)} - \rho_4]$ at iteration I is equal to the number of bonds in \mathcal{T}_2 at iteration $I - 1$, i.e., to 8^{I-1} .

Now, going from one iteration to the next ($I - 1 \rightarrow I$), two next-nearest-neighboring beads both of functionality 1 [such as in involved in the eigenmode of Fig. 2(a)] lead to two directly connected trees \mathcal{T}_1 or \mathcal{T}_2 of $I = 1$ (called leaves in the following, see Appendix). These leaves are involved in the eigenmodes, where each bead of one leaf has an opposite amplitude to that of the symmetrically equivalent bead of the other leaf. Moreover, in these modes all symmetrically equivalent beads belonging to the same leaf have the same amplitude and phase. In general, these modes lead to reduced matrices $\mathbf{A}^{(n)}(\mathcal{T}_1)$ and $\mathbf{A}^{(n)}(\mathcal{T}_2)$ whose iterative construction for $n = 2, \dots, I$ is discussed in the Appendix. The size of matrices $\mathbf{A}^{(n)}$ is

$$S(n) = \begin{cases} \frac{\sqrt{13}-1}{6\sqrt{13}}(4 + \sqrt{13})^n + \frac{\sqrt{13}+1}{6\sqrt{13}}(4 - \sqrt{13})^n & \text{for } \mathcal{T}_1, \\ \frac{\sqrt{37}-1}{6\sqrt{37}}\left(\frac{7+\sqrt{37}}{2}\right)^n + \frac{\sqrt{37}+1}{6\sqrt{37}}\left(\frac{7-\sqrt{37}}{2}\right)^n & \text{for } \mathcal{T}_2. \end{cases} \quad (13)$$

Following the above discussion, the degeneracy of each eigenvalue stemming from $\mathbf{A}^{(n)}$ appearing for the trees at iteration $I \geq n$ is

$$D(n) = \begin{cases} (3 \times 8^{I-n} + 11)/7 & \text{for } \mathcal{T}_1, \\ (4 \times 8^{I-n} + 10)/7 & \text{for } \mathcal{T}_2. \end{cases} \quad (14)$$

The size $\hat{S}(n)$ of $\hat{\mathbf{A}}^{(n)}(\mathcal{T}_2)$ is equal to $S(n)$ of \mathcal{T}_2 ,

$$\hat{S}(n) = \frac{\sqrt{37}-1}{6\sqrt{37}}\left(\frac{7+\sqrt{37}}{2}\right)^n + \frac{\sqrt{37}+1}{6\sqrt{37}}\left(\frac{7-\sqrt{37}}{2}\right)^n, \quad (15)$$

and the degeneracy of each ensuing eigenvalue at iteration $I \geq n$ is (*vide supra*)

$$\hat{D}(n) = 8^{I-n}. \quad (16)$$

Apart from matrices $\mathbf{A}^{(1)}(\mathcal{T}_1), \dots, \mathbf{A}^{(I)}(\mathcal{T}_1)$ for \mathcal{T}_1 or $\mathbf{A}^{(1)}(\mathcal{T}_2), \dots, \mathbf{A}^{(I)}(\mathcal{T}_2)$ and $\hat{\mathbf{A}}^{(1)}(\mathcal{T}_2), \dots, \hat{\mathbf{A}}^{(I)}(\mathcal{T}_2)$ for \mathcal{T}_2 , there appear for each tree (at iteration I) one matrix $\hat{\mathbf{A}}^{(I)}$ and one matrix $\mathbf{B}^{(I)}$. The size of $\hat{\mathbf{A}}^{(I)}$ is

$$\tilde{S}(I) = \begin{cases} \frac{\sqrt{13}+2}{6\sqrt{13}}(4 + \sqrt{13})^I + \frac{\sqrt{13}-2}{6\sqrt{13}}(4 - \sqrt{13})^I & \text{for } \mathcal{T}_1, \\ \frac{\sqrt{37}+5}{6\sqrt{37}}\left(\frac{7+\sqrt{37}}{2}\right)^I + \frac{\sqrt{37}-5}{6\sqrt{37}}\left(\frac{7-\sqrt{37}}{2}\right)^I & \text{for } \mathcal{T}_2, \end{cases} \quad (17)$$

and of $\mathbf{B}^{(I)}$ is

$$S_B(I) = 1 + \begin{cases} 2\tilde{S}(I) & \text{for } \mathcal{T}_1, \\ \tilde{S}(I) + \hat{S}(I) & \text{for } \mathcal{T}_2. \end{cases} \quad (18)$$

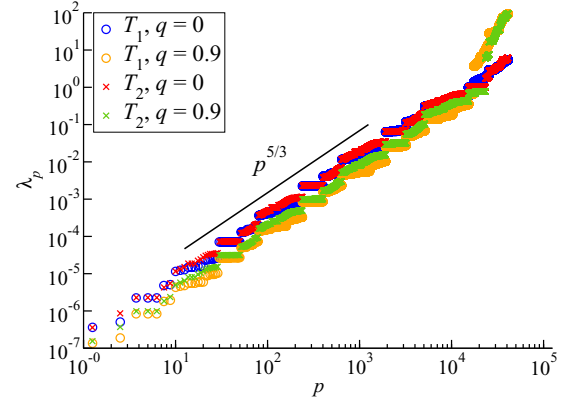


FIG. 4. Double-logarithmic representation of the eigenvalues of the dynamical matrix of \mathcal{T}_1 and \mathcal{T}_2 at iteration $I = 5$. The parameter $q = 0$ is related to fully flexible trees and $q = 0.9$ to the semiflexible ones. All spectra show for lower eigenvalues a scaling $\lambda_p \sim p^{5/3}$.

Finally, it is a simple matter to check that for \mathcal{T}_1 and \mathcal{T}_2 the total number of eigenvalues, $S_B(I) + \tilde{S}(I) + \sum_{n=1}^I D(n)S(n)$ and $S_B(I) + \tilde{S}(I) + \sum_{n=1}^I [D(n)S(n) + \hat{D}(n)\hat{S}(n)]$, respectively, is exactly equal to the number of beads at iteration I , $N(I) = 8^I + 1$. This shows that the constructed sets of eigenmodes are complete.

In Fig. 4 we exemplify the spectra for \mathcal{T}_1 and \mathcal{T}_2 having stiffness parameter $q = 0$ (fully flexible case) and $q = 0.9$ (semiflexible case). As is typical for semiflexible trees [40–43,51], switching on the stiffness leads to an increase of higher eigenvalues (due to the restricted local vibrations) and a decrease of the lower ones (due to the growth of the trees' size). Here, the lower eigenvalues scale with the mode number p as $\lambda_p \sim p^{5/3}$, notwithstanding their nonsmooth behavior reflecting the degeneracy of eigenvalues. The exponent $5/3$ is directly related to the spectral dimension $d_s = 6/5$, $2/d_s = 5/3$, which determines the scaling of density of states, $h(\lambda) \sim \lambda^{d_s/2-1}$ [20,52]. Thus, we observe that the local bending rigidity does not affect the spectral dimension.

For many quantities related to global physics the lowest eigenvalues play a major role. Looking at Fig. 4, one can observe that the lowest nonvanishing eigenvalue λ_1 is (almost) equal for \mathcal{T}_1 and \mathcal{T}_2 in case of $q = 0$ and it is slightly higher for \mathcal{T}_2 for $q = 0.9$, see also Table I. This eigenvalue comes from the matrix $\hat{\mathbf{A}}^{(I)}$ and is related to the eigenmode in which the largest branches move as whole, such as depicted in case (d) of Figs. 2 and 3 for $I = 1$. Going to the second smallest eigenvalue λ_2 , one observes large deviations between the structures; see Table I and Fig. 4. Especially in the semiflexible case ($q = 0.9$) the difference is almost given by factor two. Eigenvalue λ_2 follows from matrix $\mathbf{B}^{(I)}$ and related to the mode such as displayed in Figs. 2 and 3(h). This mode involves motion of side chains as whole that are longer in case of tree \mathcal{T}_1 leading hence for this tree to a smaller λ_2 .

IV. STATIC AND DYNAMICAL PROPERTIES OF THE TREES

Based only on the eigenvalues $\{\lambda_p\}$ of the dynamical matrix \mathbf{A} (and not on its eigenvectors), many static and

TABLE I. First two minimal nonvanishing eigenvalues of the dynamical matrix of fractal trees \mathcal{T}_1 and \mathcal{T}_2 at various iterations I and for different values of the stiffness parameter q .

I	$\lambda_1(\mathcal{T}_1)$	$\lambda_2(\mathcal{T}_1)$	$\lambda_1(\mathcal{T}_2)$	$\lambda_2(\mathcal{T}_2)$
$q = 0$				
1	0.2679	0.3446	0.2679	0.5505
2	0.01121	0.01549	0.01126	0.02641
3	0.0003651	0.0005107	0.0003663	0.0008751
4	0.00001147	0.00001607	0.00001150	0.00002754
5	3.586×10^{-7}	5.026×10^{-7}	3.597×10^{-7}	8.614×10^{-7}
$q = 0.3$				
1	0.2082	0.2505	0.2163	0.4648
2	0.008302	0.01121	0.008669	0.02039
3	0.0002698	0.0003753	0.0002806	0.0006703
4	8.477×10^{-6}	0.00001186	8.805×10^{-6}	0.00002108
5	2.651×10^{-7}	3.713×10^{-7}	2.753×10^{-7}	6.592×10^{-7}
$q = 0.6$				
1	0.1638	0.1871	0.1765	0.3989
2	0.006071	0.007997	0.006629	0.01567
3	0.0001966	0.0002716	0.0002131	0.0005091
4	6.175×10^{-6}	8.625×10^{-6}	6.680×10^{-6}	0.00001599
5	1.931×10^{-7}	2.704×10^{-7}	2.088×10^{-7}	4.999×10^{-7}
$q = 0.9$				
1	0.1305	0.1427	0.1453	0.3478
2	0.004319	0.005527	0.004990	0.01190
3	0.0001385	0.0001897	0.0001585	0.0003789
4	4.350×10^{-6}	6.062×10^{-6}	4.963×10^{-6}	0.00001188
5	1.360×10^{-7}	1.904×10^{-7}	1.551×10^{-7}	3.713×10^{-7}

dynamical properties of Gaussian polymers can be readily calculated. First, the size of a polymeric structure is typically characterized by the mean-square gyration radius $\langle R_g^2 \rangle \equiv \frac{1}{2N^2} \sum_{i,j}^N \langle (\mathbf{r}_i - \mathbf{r}_j)^2 \rangle$, which can be straightforwardly calculated from $\{\lambda_p\}$ [51,53–55]:

$$\langle R_g^2 \rangle = \frac{b^2}{N} \sum_{p=1}^{N-1} \frac{1}{\lambda_p}. \quad (19)$$

Here and in the following expressions, the sum runs over all eigenvalues, except $\lambda_0 = 0$ related to the motion of the macromolecule as whole. We note the direct relation of the mean-square gyration radius of fully flexible Gaussian trees ($q = 0$) to Wiener index, $Wi = N^2 \langle R_g^2 \rangle / b^2$; see, e.g., Ref. [56].

In Fig. 5, we plot the mean-square gyration radius $\langle R_g^2 \rangle$ of \mathcal{T}_1 and \mathcal{T}_2 as function of number of beads N . As can be inferred from the figure (solid line), both trees are compact for $I \geq 3$, i.e., $\sqrt{\langle R_g^2 \rangle} \sim N^{1/3}$ [57]. As one expects, structures with higher stiffness parameter q have higher gyration radius. Given that the lower eigenvalues play a major role for $\langle R_g^2 \rangle$, see Eq. (19), their dependency on q determines the behavior of $\langle R_g^2 \rangle$; see Figs. 4 and 5. For a given tuple (I, q) , the gyration radius of \mathcal{T}_1 is higher than for \mathcal{T}_2 . Such a behavior is quite expectable from the structure of \mathcal{T}_1 that has more beads with a longer topological distance from the core than those of \mathcal{T}_2 . This fact corresponds also to lower eigenvalues for the trees, see Fig. 4 and Table I. The significant growth of the gyration radii with increasing stiffness is due to the ground states. In

the inset to Fig. 5 we show the $\langle R_g^2 \rangle$ multiplied by λ_1 that leads to a collapse of the data for each tree. The points for \mathcal{T}_2 remain still under those of \mathcal{T}_1 due to the large difference in the second minimal nonvanishing eigenvalue λ_2 ; see Table I.

The gyration radius does not provide information about deviations from the spherical shape. For this one has to consider the eigenvalues $(\sigma_1, \sigma_2, \sigma_3)$ of the gyration tensor, such that $\sigma_1 > \sigma_2 > \sigma_3$ and $\sigma_1 + \sigma_2 + \sigma_3 = R_g^2$ hold. Based

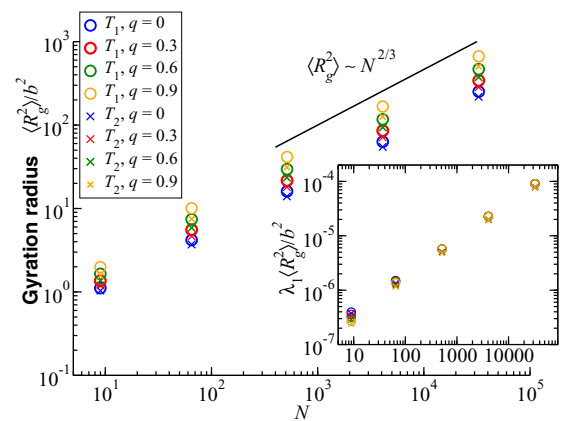


FIG. 5. Double-logarithmic representation of the mean-square gyration radii $\langle R_g^2 \rangle$ of trees \mathcal{T}_1 and \mathcal{T}_2 as function of total number of beads $N(I) = 8^I + 1$ for different values of the stiffness parameter q . Inset shows rescaled radii with the minimal nonvanishing eigenvalue λ_1 .

on $\{\sigma_i\}$, one commonly calculates [58] the average asphericity $\langle A_d \rangle$ and prolateness $\langle P_d \rangle$, which in $d = 3$ dimensions are given by [59–67]

$$\langle A_d \rangle = \left\langle \frac{\sum_{i < j}^3 (\sigma_i - \sigma_j)^2}{2R_g^4} \right\rangle \quad (20)$$

and

$$\langle P_d \rangle = \left\langle \frac{\prod_{i=1}^3 (3\sigma_i - R_g^2)}{2R_g^6} \right\rangle. \quad (21)$$

The limiting values for asphericity $\langle A_d \rangle$ are 0 for spherical shape and 1 for rodlike shape. The prolateness $\langle P_d \rangle$ takes negative values from $(-1/8, 0)$ for oblate shapes and positive values from $(0, 1)$ for prolate shapes. As for asphericity, if prolateness is zero, then the shape of the structure is spherical [59–67]. In the dimension $d = 3$ the average asphericity $\langle A_d \rangle$ and the average prolateness $\langle P_d \rangle$ read [61–63, 65, 66]

$$\langle A_d \rangle = \frac{15}{2} \int_0^\infty dy \sum_{k=1}^{N-1} \frac{y^3}{(\lambda_k + y^2)^2} \left[\prod_{j=1}^{N-1} \frac{\lambda_j}{\lambda_j + y^2} \right]^{\frac{3}{2}} \quad (22)$$

and

$$\langle P_d \rangle = \frac{105}{8} \int_0^\infty dy \sum_{k=1}^{N-1} \frac{y^5}{(\lambda_k + y^2)^3} \left[\prod_{j=1}^{N-1} \frac{\lambda_j}{\lambda_j + y^2} \right]^{\frac{3}{2}}, \quad (23)$$

respectively.

In Fig. 6 we plot average asphericity $\langle A_d \rangle$ and prolateness $\langle P_d \rangle$ for trees \mathcal{T}_1 and \mathcal{T}_2 of different size $N(I)$ and stiffness q . First, one can see that both trees have an aspheric shape that for high iterations I saturates to an universal value $\langle A_d \rangle \simeq 0.22$ for all considered values of q . Thus, the trees are less aspherical than ideal linear chains [60, 67] or combs [63, 66] and more aspherical than ideal stars with $f > 4$ arms [63]. Furthermore, both trees \mathcal{T}_1 and \mathcal{T}_2 are prolate, given that $\langle P_d \rangle > 0$. For larger iterations, the data collapse for all considered values of q on $\langle P_d \rangle \simeq 0.088$ for \mathcal{T}_1 and $\langle P_d \rangle \simeq 0.092$ for \mathcal{T}_2 . The latter prolateness value of 0.092 for \mathcal{T}_2 is close to that of the four-arm star [63]. Tree \mathcal{T}_1 is less prolate (that is also evident from the topology of the tree, Fig. 1), the corresponding value 0.088 lies between that of the four-arm and five-arm stars [63].

While the mean-square gyration radius and the shape parameters can be calculated based on the eigenvalues only, for many quantities more information about the structures is needed. Here we consider the equilibrium density of contacts and the form factors of the trees. Both characteristics can be calculated based on the matrix of equilibrium mean-square distances $\mathbf{L} = (L_{ij})$, where L_{ij} gives the mean-square distance between monomers i and j (in the units of b^2). The matrix \mathbf{L} is directly related to the (symmetric) dynamical matrix \mathbf{A} by [68–70]

$$L_{ij} = A_{ii}^\dagger + A_{jj}^\dagger - 2A_{ij}^\dagger, \quad (24)$$

where $\{A_{ij}^\dagger\}$ are the elements of the Moore-Penrose pseudoinverse matrix \mathbf{A}^\dagger of \mathbf{A} . Given that the singularity of the matrix \mathbf{A} comes from the translational mode $\mathbf{v}_0 = (1, 1, \dots, 1)^T / \sqrt{N}$ [such as depicted in Figs. 2 and 3(i)] that leads to the eigenvalue

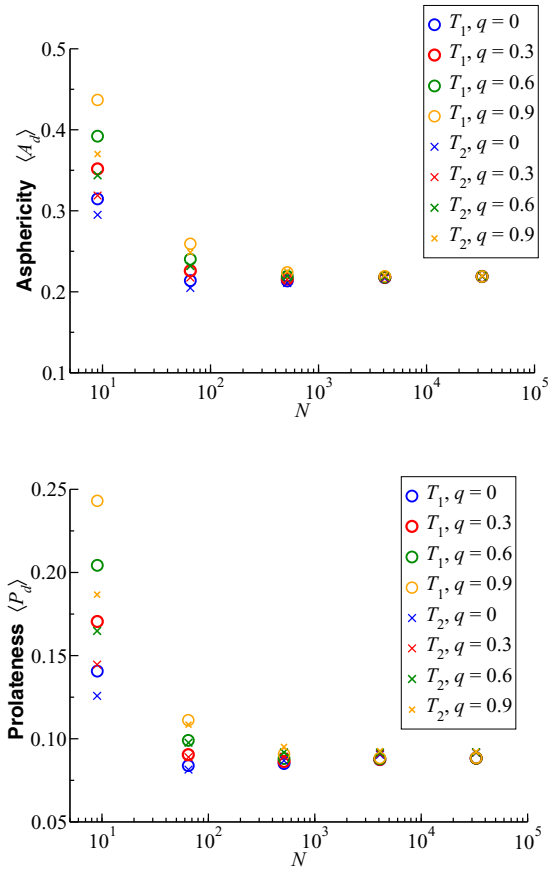


FIG. 6. Half-logarithmic representation of the asphericity $\langle A_d \rangle$ and prolateness $\langle P_d \rangle$ of trees \mathcal{T}_1 and \mathcal{T}_2 as function of total number of beads $N(I) = 8^I + 1$ for different values of the stiffness parameter q . As expected for large self-similar objects (here for $N > 500$), both characteristics saturate to a plateau.

$\lambda_0 = 0$, the pseudoinverse of \mathbf{A} can be readily computed,

$$\mathbf{A}^\dagger = (\mathbf{A} - \mathbf{v}_0 \otimes \mathbf{v}_0)^{-1} + \mathbf{v}_0 \otimes \mathbf{v}_0. \quad (25)$$

Now, the probability p_{ij} that two monomers (say, i and j) are in contact is given by $p_{ij} = (2\pi L_{ij}/3)^{-3/2}$ [36]. With this, the contact density (i.e., number of contacts per monomer) reads

$$\hat{\rho}_c = \frac{1}{N} \sum_{i < j} \left(\frac{3}{2\pi L_{ij}} \right)^{3/2}. \quad (26)$$

In Fig. 7 we show the contact density for different values of stiffness parameter q . Introducing stiffness leads to a tremendous reduction of the number of contacts. Moreover, this effect is more striking for larger trees. For fully flexible ($q = 0$) tree \mathcal{T}_1 at iteration $I = 4$ the number of contacts per bead is higher than 2, whereas introducing semiflexibility to this tree leads, e.g., for $q = 0.9$, to less than one contact per bead. Generally, tree \mathcal{T}_1 has lower contact density than \mathcal{T}_2 of the same size N and stiffness q . This observation corresponds to the higher gyration radius of \mathcal{T}_1 in comparison to \mathcal{T}_2 ; see Fig. 5.

The internal organization of macromolecules is studied in scattering experiments by looking at the coherent intramolecular form factor $F(k) = \frac{1}{N} \sum_{i,j} \langle \exp[i\mathbf{k} \cdot (\mathbf{r}_i - \mathbf{r}_j)] \rangle$.

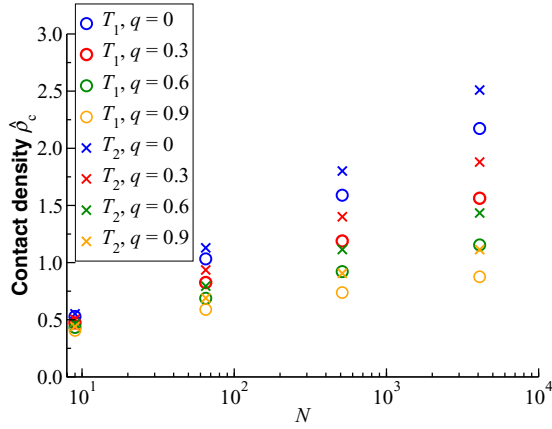


FIG. 7. Half-logarithmic representation of the number of self-contacts per monomer for trees \mathcal{T}_1 and \mathcal{T}_2 as function of total number of beads $N(I) = 8^I + 1$ for different values of the stiffness parameter q .

For Gaussian distributed $\{\mathbf{r}_i\}$, the form factor $F(k)$ can be formulated in terms of the distance matrix \mathbf{L} [36],

$$F(k) = \frac{1}{N} \sum_{i,j} \exp \left[-\frac{k^2 b^2}{6} L_{ij} \right]. \quad (27)$$

In Fig. 8 we plot the form factor of trees \mathcal{T}_1 and \mathcal{T}_2 at iteration $I = 4$ for different values of the stiffness parameter q using Kratky representation. Moreover, we rescale the wave vector by taking $Q = k\sqrt{\langle R_g^2 \rangle}$. In this representation all data for $Q \lesssim 4$ collapse. For higher Q the data for stiffer structures lie above those of the flexible ones, reflecting more swollen local organization of the trees. In the intermediate region of $1 < Q < 10$ the data approach scaling, $F(k) \sim k^{-3}$. The differences at rather large $Q \simeq 10$ reflect their local character, hence for higher iterations I they are expected to be less relevant.

We close the discussion of static properties of the trees and proceed to the dynamics of the structures. First, we consider

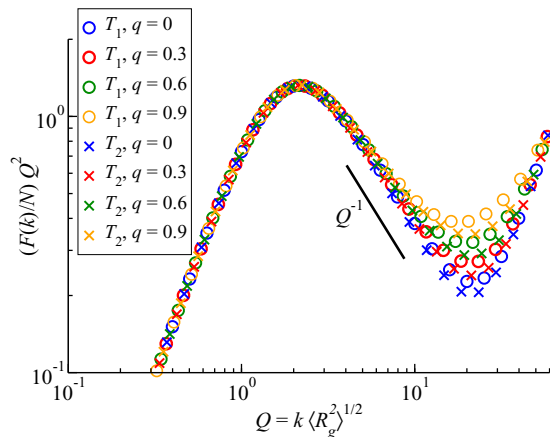


FIG. 8. Kratky representation $k^2 F(k)$ of the form factor of trees \mathcal{T}_1 and \mathcal{T}_2 at iteration $I = 4$ for different values of the stiffness parameter q . In the intermediate region of $Q = k\sqrt{\langle R_g^2 \rangle}$, the data saturate on the scaling Q^{-1} .

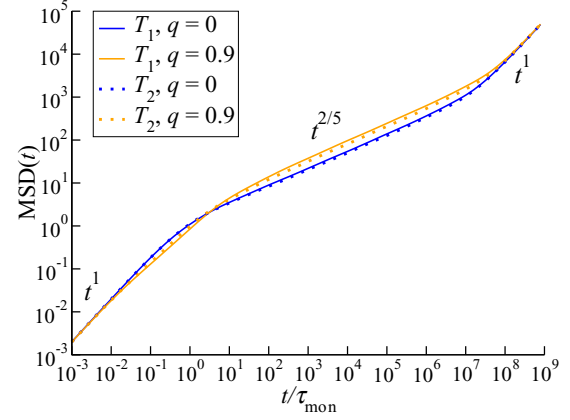


FIG. 9. Double-logarithmic representation of the monomeric MSD for trees \mathcal{T}_1 and \mathcal{T}_2 at iteration $I = 5$ having different values of stiffness parameter q .

the mean-square displacement (MSD) of monomers averaged over the whole structure that follows from Eq. (2) and is given by [35,36]

$$\overline{\langle (\mathbf{r}(t) - \mathbf{r}(0))^2 \rangle} = \frac{2b^2}{N} \left(\frac{t}{\tau_{\text{mon}}} + \sum_{p=1}^{N-1} \frac{1 - e^{-t\lambda_p/\tau_{\text{mon}}}}{\lambda_p} \right), \quad (28)$$

where $\langle \dots \rangle$ and $\overline{\dots}$ denote conformational and structural averages, respectively, and $\tau_{\text{mon}} = \zeta b^2 / 3k_B T$ is the monomeric relaxation time. The results for MSD of the trees at iteration $I = 5$ are presented in Fig. 9. Apart from evident scaling t^1 for $t \ll \tau_{\text{mon}}$ and $t \gg \tau_{\text{mon}} N^{5/3}$, there is subdiffusion $t^{2/5}$ at intermediate times. The exponent $2/5$ is closely related to the spectral dimension $d_s = 6/5$ [20]: The relation $2/5 = 1 - d_s/2$ follows straightforwardly from Eq. (28) if one replaces there the sum through an integral, $\sum \dots \rightarrow \int d\lambda h(\lambda) \dots$, where $h(\lambda) \sim \lambda^{d_s/2-1}$ is the density of states. The subdiffusive exponent is robust under introduction of stiffness, and the MSD of beads belonging to stiffer structures is slightly higher at intermediate times.

In the mechanical relaxation experiments one measures responses to external strain fields. The typical response function is the shear relaxation modulus that follows for Gaussian macromolecules the relation [35,36,54]

$$G(t) = \frac{ck_B T}{(N-1)} \sum_{p=1}^{N-1} \exp \left[-\frac{2\lambda_p t}{\tau_{\text{mon}}} \right], \quad (29)$$

where c is the number density of the segments. The development of $G(t)$ with time is exemplified for trees \mathcal{T}_1 and \mathcal{T}_2 on Fig. 10. Also there we plot experimentally relevant frequency representatives of $G(t)$, the storage $G'(\omega)$ and loss $G''(\omega)$ moduli [36],

$$G'(\omega) = \frac{ck_B T}{(N-1)} \sum_{p=1}^{N-1} \frac{(\omega\tau_{\text{mon}}/2\lambda_p)^2}{1 + (\omega\tau_{\text{mon}}/2\lambda_p)^2} \quad (30)$$

and

$$G''(\omega) = \frac{ck_B T}{(N-1)} \sum_{p=1}^{N-1} \frac{\omega\tau_{\text{mon}}/2\lambda_p}{1 + (\omega\tau_{\text{mon}}/2\lambda_p)^2}. \quad (31)$$

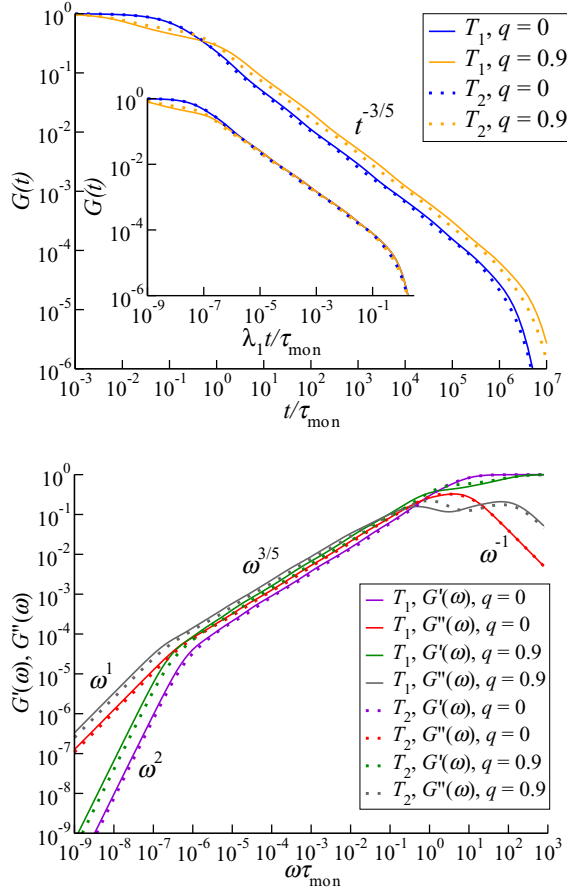


FIG. 10. Top: Double-logarithmic representation of the shear-stress relaxation modulus $G(t)$ for trees \mathcal{T}_1 and \mathcal{T}_2 at iteration $I = 5$ having different values of stiffness parameter q . Inset shows $G(t)$ with rescaled by factor λ_1 time. Bottom: Double-logarithmic representation of the storage $G'(\omega)$ and loss $G''(\omega)$ moduli corresponding to $G(t)$ of the main top plot. For all curves $ck_B T = 1$ is taken.

The initial value of the shear-stress relaxation modulus, $G(t = 0^+) = ck_B T$, is given by the affine shear elasticity of a system of ideal springs [71]. At the intermediate times the $G(t)$ decays algebraically (here with the exponent $-3/5 = -d_s/2$) that readily follows from the behavior of the density of states $h(\lambda)$ [20]. At long times due to the finite size of structures, one gets an exponential cutoff related to the minimal eigenvalue λ_1 ; see Table I. Exceptionally at initial times, the $G(t)$ for semiflexible ($q = 0.9$) trees decays faster than that of the flexible trees $q = 0$. (One finds corresponding deviations for $G'(\omega)$ or $G''(\omega)$ at high frequencies.) This behavior shows fast local vibrations in semiflexible trees due to the locally restricted bonds that are also manifested in the eigenvalues for large mode number p in Fig. 4. Correspondingly to the behavior of $G(t)$, at very low frequencies, $\omega\tau_{\text{mon}} \ll N^{-5/3}$, one finds $G'(\omega) \sim \omega^2$ and $G''(\omega) \sim \omega$; at very high frequencies one has $G'(\omega) \rightarrow ck_B T$ and $G''(\omega) \sim \omega^{-1}$ [36]. Moreover, as one expects for self-similar fractal objects of spectral dimension d_s , we find in the intermediate frequency regime that

$$G'(\omega) \approx G''(\omega) \sim \omega^{d_s/2}. \quad (32)$$

V. SUMMARY AND CONCLUSIONS

In summary, in this work we have studied marginally compact trees that are created by means of two fractal generators. We focused on the role of local stiffness for the typical static and dynamical characteristics of the trees. We have shown that introduction of stiffness leads to an increase of size R of the structures. Nevertheless, the structures remain compact, by showing a $R \sim N^{1/3}$ scaling. Moreover, the static form factor approaches for large structures an intermediate $F(k) \sim k^{-3}$ behavior. The ensuing exponent can be assigned, from one side, to the fractal dimension $d_f = 3$ and, from another side, to a fractal surface with dimension $d_A = 3$. (We note that the objects with a smooth surface, e.g., a ball, have $d_A = 2$.) Furthermore, the shape of the trees is not spherical and the corresponding asphericity and prolateness parameters for large-enough structures are independent of the stiffness and the tree structure. At the same time the semiflexibility influences tremendously the density of self-contacts that gets drastically reduced with growing stiffness. In the dynamics, the scaling of the relaxation times, $\tau_p \sim (N/p)^{5/3}$, is reflected in the monomeric mean-square displacement or in the shear-stress relaxation modulus by showing at intermediate times the behavior $t^{2/5}$ or $t^{-3/5}$, respectively.

Coming back to recent paper [20] by some of us, where we have shown that the linear spacers reduce the number of contacts, here we have suggested another recipe for suppression of the self-contact density by introducing local stiffness. We note that so far these findings were demonstrated for ideal trees. In this respect it will be interesting to look on the excluded volume and finite extensibility effects in the future.

ACKNOWLEDGMENTS

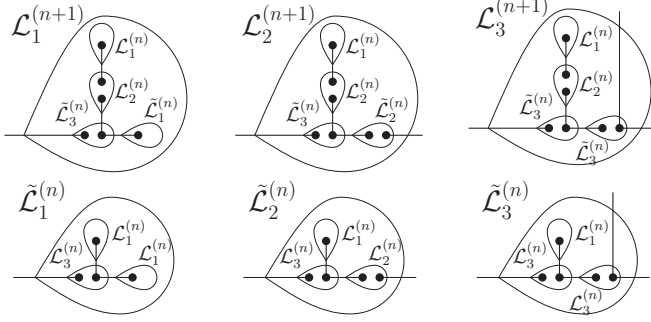
The authors thank A. Blumen and J.-U. Sommer for fruitful discussions. M.D. acknowledges DFG through GRK 1642/1.

APPENDIX: STRUCTURE OF EIGENMODES AND CORRESPONDING REDUCED MATRICES

1. Tree \mathcal{T}_1

a. Number of distinct amplitudes

As has been discussed in the main part of the paper, the symmetry of \mathcal{T}_1 allows a construction of eigenmodes in which some beads move with the same amplitude. The number of the distinct nonvanishing amplitudes determines then the size of reduced matrices, which are, e.g., for $I = 1$ presented by Eqs. (6)–(8). Now, at higher iterations I one gets a similar pattern of motion as in Fig. 2(a) and 2(b), where two directly connected substructures (called “leaves,” see $\mathcal{L}_1^{(n+1)}$ in Fig. 11) move against each other. The modes of Fig. 2(c) and 2(d) bring forth at iteration I the pattern in which two leaves $\tilde{\mathcal{L}}_1^{(I)}$ (see Fig. 11) move against each other. Each such a leaf, \mathcal{L}_i or $\tilde{\mathcal{L}}_i$, can be constructed in an iterative way from other leaves \mathcal{L}_i or $\tilde{\mathcal{L}}_i$ (index i indicates that $i - 1$ outer leaves are connected to \mathcal{L}_i or to $\tilde{\mathcal{L}}_i$), see Fig. 11. This construction allows to calculate the number of distinct amplitudes $S(n)$ or $\tilde{S}(n)$ in the modes involving leaves $\mathcal{L}_1^{(n)}$ or $\tilde{\mathcal{L}}_1^{(n)}$, which give the size of matrices $\mathbf{A}^{(n)}$ or $\tilde{\mathbf{A}}^{(n)}$, respectively.


 FIG. 11. Schematic sketch of substructures (“leaves” \mathcal{L}) of tree \mathcal{T}_1 .

We start by looking at $\tilde{S}(n)$. The corresponding leaf $\tilde{\mathcal{L}}_1^{(n)}$ consists of one leaf $\mathcal{L}_3^{(n)}$ and two $\mathcal{L}_1^{(n)}$. There, the beads of one leaf $\mathcal{L}_1^{(n)}$ move with exactly the same amplitude and phase as by their symmetric counterparts in the other leaf $\mathcal{L}_1^{(n)}$ [see Fig. 2(c) and 2(d) for $n = 1$]. Therefore, the presence of the second leaf $\mathcal{L}_1^{(n)}$ does not increase $\tilde{S}(n)$. Denoting by $S'(n)$ the number of independent amplitudes coming from $\mathcal{L}_3^{(n)}$, we then get

$$\tilde{S}(n) = S(n) + S'(n). \quad (\text{A1})$$

In a similar way, by looking at $\mathcal{L}_1^{(n+1)}$ in Fig. 11 and using Eq. (A1), we obtain the number $S(n)$ of independent amplitudes coming from $\mathcal{L}_1^{(n)}$,

$$S(n) = 3S(n-1) + 4S'(n-1), \quad (\text{A2})$$

where we have used that leaves $\mathcal{L}_2^{(n-1)}$ and $\mathcal{L}_3^{(n-1)}$ bring the same number of independent amplitudes $S'(n)$. Equations (A1)

$$\mathbf{A}^{(2)} = \begin{pmatrix} \mu_3^{(1)} + \rho_2 & v_{13} & 0 & 0 & \rho_3 & 0 & 0 \\ 2v_{13} & \mu_{113}^{(3)} & 0 & \rho_3 & v_{33} & 0 & \rho_3 \\ 0 & 0 & \mu_2^{(1)} & v_{13} & \rho_2 & 0 & 0 \\ 0 & \rho_3 & v_{12} & \mu_{13}^{(2)} & v_{23} & 0 & \rho_3 \\ 2\rho_3 & v_{33} & \rho_2 & v_{23} & \mu_{233}^{(3)} & \rho_3 & v_{33} \\ 0 & 0 & 0 & 0 & \rho_3 & \mu_3^{(1)} & v_{13} \\ 0 & \rho_3 & 0 & \rho_3 & v_{33} & v_{13} & \mu_{133}^{(3)} - \rho_3 \end{pmatrix}$$

related to an antiphase motion of two neighboring $\mathcal{L}_1^{(2)}$ leaves and on the auxiliary matrix

$$\mathbf{H}_1^{(2)} = \begin{pmatrix} \mu_{333}^{(3)} & \rho_3 & v_{33} & 0 & 0 & \rho_3 & 0 & 0 \\ \rho_3 & \mu_3^{(1)} & v_{13} & 0 & 0 & \rho_3 & 0 & 0 \\ v_{33} & v_{13} & \mu_{13}^{(2)} & 0 & \rho_3 & v_{33} & 0 & \rho_3 \\ 0 & 0 & 0 & \mu_2^{(1)} & v_{12} & \rho_2 & 0 & 0 \\ 0 & 0 & \rho_3 & v_{12} & \mu_{13}^{(2)} & v_{23} & 0 & \rho_3 \\ \rho_3 & \rho_3 & v_{33} & \rho_2 & v_{23} & \mu_{233}^{(3)} & \rho_3 & v_{33} \\ 0 & 0 & 0 & 0 & 0 & \rho_3 & \mu_3^{(1)} & v_{13} \\ 0 & 0 & \rho_3 & 0 & \rho_3 & v_{33} & v_{13} & \mu_{133}^{(3)} - \rho_3 \end{pmatrix}.$$

and (A2) involve $S'(n)$, for which the recurrent equation

$$S'(n) = 3S(n-1) + 5S'(n-1) \quad (\text{A3})$$

holds, as can be found by inspecting $\mathcal{L}_2^{(n+1)}$ or $\mathcal{L}_3^{(n+1)}$ of Fig. 11.

In order to solve the set of recurrent Eqs. (A1)–(A3), we first subtract (A2) from (A3), $S'(n) - S(n) = S'(n-1)$, from which follows that

$$S'(n) = \sum_{i=1}^n S(i) \quad (\text{A4})$$

and that

$$S(n) = 8S(n-1) - 3S(n-2). \quad (\text{A5})$$

The solution of Eq. (A5) with initial conditions $S(1) = 1$ and $S(2) = 7$ is

$$S(n) = \frac{\sqrt{13}-1}{6\sqrt{13}}(4+\sqrt{13})^n + \frac{\sqrt{13}+1}{6\sqrt{13}}(4-\sqrt{13})^n. \quad (\text{A6})$$

Based on this result and on employment of Eqs. (A1) and (A4), the other quantities $\tilde{S}(n)$ and $S'(n)$ can be readily calculated [the result for $\tilde{S}(n)$ is given in Eq. (17) of the main text].

Finally, we discuss the size of matrix $\mathbf{B}^{(I)}$, that is coming from the modes in which all beads are moving. Here helps the observation that tree \mathcal{T}_1 at iteration I consists from two equivalent leaves $\tilde{\mathcal{L}}_1^{(I)}$ that are connected through the core bead to leaf $\mathcal{L}_2^{(I)}$, which is also then connected to a leaf $\mathcal{L}_1^{(I)}$. With this the size of $\mathbf{B}^{(I)}$, $S_B(I)$, reads:

$$S_B(I) = \tilde{S}(I) + S(I) + S'(I) + 1 \quad (\text{A7})$$

so that, together with Eq. (A1), Eq. (18) for \mathcal{T}_1 follows.

b. Initial matrices

Starting with $I \geq 2$ the next-nearest-neighboring interactions affect only directly connected leaves. Thus, it is sufficient to initialize iterative construction of reduced matrices based on

c. Construction of $\tilde{\mathbf{A}}^{(I)}$

By investigation of Fig. 11, one can see that an $\tilde{\mathcal{L}}_1$ leaf is formed by three subunits, from which two are symmetrically equivalent. Consequently, they are described by the same matrix. Therefore, the corresponding matrix $\tilde{\mathbf{A}}^{(I)}$ has the shape

$$\tilde{\mathbf{A}}^{(I)} = \begin{pmatrix} \boldsymbol{\alpha} & \mathbf{C}_{12} \\ \mathbf{C}_{21} & \boldsymbol{\beta} \end{pmatrix}. \quad (\text{A8})$$

Here $\boldsymbol{\alpha}$ represents the cophase movement of two \mathcal{L}_1 leaves, which makes it very similar to the matrix $\mathbf{A}^{(I)}$: The only difference is in the last diagonal element describing the amplitude numbered by $S(I)$:

$$(\boldsymbol{\alpha})_{ij} = \begin{cases} \mu_{133}^{(3)} + \rho_3 & (i, j) = (S(I), S(I)) \\ (\mathbf{A}_1^{(I)})_{ij} & \text{otherwise} \end{cases}, \quad (\text{A9})$$

Furthermore, in Eq. (A8) $\boldsymbol{\beta}$ describes the dynamics of the less symmetric \mathcal{L}_3 leaf,

$$(\boldsymbol{\beta})_{ij} = \begin{cases} \mu_{133}^{(3)} & (i, j) = (\tilde{S}'(I-1), \tilde{S}'(I-1)) \\ (\mathbf{H}_1^{(I)})_{ij} & \text{otherwise} \end{cases}, \quad (\text{A10})$$

where $\tilde{S}'(I-1) = \tilde{S}(I-1) + S'(I-1)$ and

$$\mathbf{H}_1^{(I)} = \begin{pmatrix} \zeta & 0 & \mathbf{E}_{13} & \mathbf{E}_{14} \\ 0 & \delta & \mathbf{E}_{23} & 0 \\ \mathbf{E}_{13}^T & \mathbf{E}_{23}^T & \epsilon & \mathbf{E}_{34} \\ \mathbf{E}_{14}^T & 0 & \mathbf{E}_{34}^T & \zeta \end{pmatrix}. \quad (\text{A11})$$

Here ζ stands for the antiphase movement of two \mathcal{L}_3 leaves and δ or ϵ describe isolated (i.e., that do not have a symmetrically equivalent neighboring partner) leaves \mathcal{L}_1 or \mathcal{L}_2 , respectively. The structure of these blocks is provided in Eqs. (A14), (A15), and (A17), *vide infra*. The interactions between these leaves are described by very sparse matrices $\mathbf{E}_{ji} = \mathbf{E}_{ij}^T$:

$$\begin{aligned} (\mathbf{E}_{13})_{ij} &= \begin{cases} \rho_3 & (i, j) = (\tilde{S}'(I), S'(I)) \\ 0 & \text{otherwise,} \end{cases} \\ (\mathbf{E}_{14})_{ij} &= \begin{cases} v_{33} & (i, j) = (\tilde{S}'(I), 1) \\ \rho_3 & (i, j) \in \{(\tilde{S}'(I), 3), (\tilde{S}'(I) - 1, 1), \\ & \quad (\tilde{S}'(I) - 2, 1)\} \\ 0 & \text{otherwise,} \end{cases} \\ (\mathbf{E}_{23})_{ij} &= \begin{cases} v_{23} & (i, j) = (S(I), 1) \\ \rho_2 & (i, j) = (S(I), 3) \\ \rho_3 & (i, j) \in \{(S(I) - 1, 1), (S(I) - 2, 1)\} \\ 0 & \text{otherwise,} \end{cases} \\ (\mathbf{E}_{34})_{ij} &= \begin{cases} v_{33} & (i, j) = (S'(I), 1) \\ \rho_3 & (i, j) \in \{(S'(I), 3), (S'(I) - 1, 1), \\ & \quad (S'(I) - 2, 1)\} \\ 0 & \text{otherwise.} \end{cases} \end{aligned}$$

Finally, the off-diagonal matrices \mathbf{C}_{12} and \mathbf{C}_{21} in Eq. (A8) are

$$(\mathbf{C}_{12})_{ij} = \begin{cases} v_{33} & (i, j) = (S(I), 1) \\ \rho_3 & (i, j) \in \{(S(I) - 1, 1), (S(I) - 2, 1), \\ & \quad (S(I), 3)\} \\ 0 & \text{otherwise} \end{cases}$$

and $\mathbf{C}_{21} = 2\mathbf{C}_{12}^T$.

d. Construction of $\mathbf{A}^{(I+1)}$

As can be inferred from Fig. 2, leaf \mathcal{L}_1 consists from leaves $\tilde{\mathcal{L}}_1$, \mathcal{L}_1 , \mathcal{L}_2 , and $\tilde{\mathcal{L}}_3$ of the previous iteration. With this, the matrix describing antiphase motion of two directly connected $\mathcal{L}_1^{(I+1)}$ leaves is given by

$$\mathbf{A}^{(I+1)} = \begin{pmatrix} \boldsymbol{\gamma} & 0 & \mathbf{D}_{13} & \mathbf{D}_{14} \\ 0 & \delta & \mathbf{D}_{23} & 0 \\ \mathbf{D}_{12}^T & \mathbf{D}_{23}^T & \epsilon & \mathbf{D}_{34} \\ \mathbf{D}_{14}^T & 0 & \mathbf{D}_{34}^T & \zeta \end{pmatrix}. \quad (\text{A12})$$

Here $\boldsymbol{\gamma}$ describes the movement of an isolated $\tilde{\mathcal{L}}_1^{(I)}$ leaf. With a small modification concerning its last bead having number $\tilde{S}(I)$, we can obtain an expression for $\boldsymbol{\gamma}$:

$$(\boldsymbol{\gamma})_{ij} = \begin{cases} \mu_{133}^{(3)} & (i, j) = (\tilde{S}(I), \tilde{S}(I)) \\ (\tilde{\mathbf{A}}^{(I)})_{ij} & \text{otherwise} \end{cases}. \quad (\text{A13})$$

The other matrices δ , ϵ , and ζ standing for the remaining \mathcal{L}_1 , \mathcal{L}_2 , and $\tilde{\mathcal{L}}_3$ leaves, respectively, can be constructed as follows. Matrix δ describes the dynamics of an isolated \mathcal{L}_1 leaf, in a similar fashion as for $\boldsymbol{\gamma}$, δ follows from $\mathbf{A}^{(I)}$:

$$(\delta)_{ij} = \begin{cases} \mu_{123}^{(3)} & (i, j) = (S(I), S(I)) \\ (\mathbf{A}^{(I)})_{ij} & \text{otherwise} \end{cases}. \quad (\text{A14})$$

Matrix ϵ reflects the dynamics of an isolated \mathcal{L}_2 leave, which is less symmetric than $\tilde{\mathcal{L}}_1$ or \mathcal{L}_1 . Its similarity to an \mathcal{L}_3 leaf makes it possible to reuse the helper matrix $\mathbf{H}_1^{(I-1)}$:

$$(\epsilon)_{ij} = \begin{cases} \mu_{33}^{(2)} & (i, j) = (1, 1) \\ \mu_{123}^{(3)} & (i, j) = (3, 3) \\ v_{23} & (i, j) \in \{(1, 3), (3, 1)\} \\ \mu_{133}^{(3)} & (i, j) = (S'(I), S'(I)) \\ (\mathbf{H}_1^{(I-1)})_{ij} & \text{otherwise} \end{cases}. \quad (\text{A15})$$

Finally, the $\tilde{\mathcal{L}}_3$ leaf represented by ζ in Eq. (A12) has a high similarity to the previously discussed $\tilde{\mathcal{L}}_1$ leaf. We introduce another helper matrix,

$$\mathbf{H}_2^{(I)} = \begin{pmatrix} \boldsymbol{\beta} & \mathbf{F}_{12} & \mathbf{F}_{13} \\ \mathbf{F}_{12}^T & \boldsymbol{\alpha} & \mathbf{F}_{23} \\ \mathbf{F}_{13}^T & \mathbf{F}_{23}^T & \boldsymbol{\beta} \end{pmatrix}. \quad (\text{A16})$$

With only one small modification one can now obtain $\boldsymbol{\zeta}$:

$$(\boldsymbol{\zeta})_{ij} = \begin{cases} \mu_{133}^{(3)} & (i, j) \in \{(S'(I-1), S'(I-1)), \\ & \quad (\tilde{S}(I-1), \tilde{S}(I-1))\} \\ (\mathbf{H}_2^{(I)})_{ij} & \text{otherwise} \end{cases}. \quad (\text{A17})$$

The interaction matrices follow readily, keeping in mind that $\mathbf{F}_{ij} = \mathbf{F}_{ji}^T$ and $\mathbf{D}_{ij} = \mathbf{D}_{ji}^T$,

$$(\mathbf{F}_{12})_{ij} = \begin{cases} \rho_3 & (i, j) = (S'(I), S(I)) \\ 0 & \text{otherwise} \end{cases},$$

$$(\mathbf{F}_{13})_{ij} = \begin{cases} \nu_{33} & (i, j) = (S'(I), 1) \\ \rho_3 & (i, j) \in \{(S'(I), 3), (S'(I) - 1, 1), \\ & (S'(I) - 2, 1)\} \\ 0 & \text{otherwise} \end{cases},$$

$$(\mathbf{F}_{23})_{ij} = \begin{cases} \nu_{33} & (i, j) = (S(I), 1) \\ \rho_3 & (i, j) \in \{(S(I), 3), (S(I) - 1, 1), \\ & (S(I) - 2, 1)\} \\ 0 & \text{otherwise} \end{cases},$$

and

$$(\mathbf{D}_{13})_{ij} = \begin{cases} \rho_3 & (i, j) = (\tilde{S}(I), S'(I)) \\ 0 & \text{otherwise} \end{cases},$$

$$(\mathbf{D}_{14})_{ij} = \begin{cases} \nu_{33} & (i, j) = (\tilde{S}(I), 1) \\ \rho_3 & (i, j) \in \{(\tilde{S}(I) - 1, 1), (\tilde{S}(I) - 2, 1), \\ & (\tilde{S}(I), 3)\} \\ 0 & \text{otherwise} \end{cases},$$

$$(\mathbf{D}_{23})_{ij} = \begin{cases} \nu_{23} & (i, j) = (S(I), 1) \\ \rho_2 & (i, j) = (S(I), 3) \\ \rho_3 & (i, j) \in \{(S(I) - 1, 1), (S(I) - 2, 1)\} \\ 0 & \text{otherwise} \end{cases},$$

$$(\mathbf{D}_{34})_{ij} = \begin{cases} \nu_{33} & (i, j) = (S'(I), 1) \\ \rho_3 & (i, j) \in \{(S'(I), 3), (S'(I) - 1, 1), \\ & (S'(I) - 2, 1)\} \\ 0 & \text{otherwise} \end{cases}.$$

e. Construction of $\mathbf{B}^{(I+1)}$

The matrix \mathbf{B} describes identical motion of all symmetrically equivalent beads. Now, one can split \mathcal{T}_1 into two $\tilde{\mathcal{L}}_1$ leaves, one \mathcal{L}_1 and one \mathcal{L}_2 leaf as well as the core bead. Therefore, its structure reads

$$\mathbf{B}^{(I+1)} = \begin{pmatrix} \eta & 0 & \mathbf{G}_{13} & \mathbf{G}_{14} \\ 0 & \delta & \mathbf{G}_{23} & 0 \\ \mathbf{G}_{31} & \mathbf{G}_{32} & \epsilon & \mathbf{G}_{34} \\ \mathbf{G}_{41} & 0 & \mathbf{G}_{43} & \mu_{333}^{(3)} \end{pmatrix}, \quad (\text{A18})$$

where η represents a cophase motion of two $\tilde{\mathcal{L}}_1$ leaves, with the only difference to $\tilde{\mathbf{A}}^{(I)}$ being in one entry,

$$(\eta)_{ij} = \begin{cases} \mu_{133}^{(3)} + \rho_3 & (i, j) = (\tilde{S}(I), \tilde{S}(I)) \\ (\tilde{\mathbf{A}}^{(I)})_{ij} & \text{otherwise} \end{cases}. \quad (\text{A19})$$

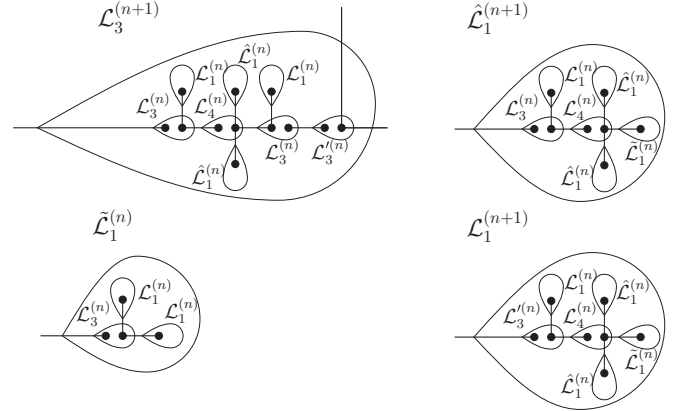


FIG. 12. Schematic sketch of substructures (“leaves” \mathcal{L}) of tree \mathcal{T}_2 .

The other diagonal blocks are given in Eqs. (A14) and (A15). The off-diagonal blocks are as follows:

$$(\mathbf{G}_{13})_{ij} = \begin{cases} \rho_3 & (i, j) = (\tilde{S}(I), S'(I)) \\ 0 & \text{otherwise} \end{cases},$$

$$(\mathbf{G}_{14})_{ij} = \begin{cases} \nu_{33} & (i, j) = (\tilde{S}(I), 1) \\ \rho_3 & (i, j) \in \{(\tilde{S}(I) - 1, 1), (\tilde{S}(I) - 2, 1)\} \\ 0 & \text{otherwise} \end{cases},$$

$$(\mathbf{G}_{23})_{ij} = \begin{cases} \nu_{23} & (i, j) = (S(I), 1) \\ \rho_2 & (i, j) = (S(I), 3) \\ \rho_3 & (i, j) \in \{(S(I) - 1, 1), (S(I) - 2, 1)\} \\ 0 & \text{otherwise} \end{cases},$$

$$(\mathbf{G}_{34})_{ij} = \begin{cases} \nu_{33} & (i, j) = (S'(I), 1) \\ \rho_3 & (i, j) \in \{(S'(I) - 1, 1), (S'(I) - 2, 1)\} \\ 0 & \text{otherwise} \end{cases}.$$

Furthermore, $\mathbf{G}_{31} = 2\mathbf{G}_{13}^T$, $\mathbf{G}_{41} = 2\mathbf{G}_{14}^T$, $\mathbf{G}_{32} = \mathbf{G}_{23}^T$, and $\mathbf{G}_{43} = \mathbf{G}_{34}^T$.

2. Tree \mathcal{T}_2

a. Number of distinct amplitudes

As for tree \mathcal{T}_1 , for \mathcal{T}_2 the number of distinct amplitudes in a given mode (that is then equal to the size of the corresponding reduced matrices) can be calculated by observation of the iterative construction of leaves (Fig. 12).

The tree \mathcal{T}_2 at iteration $I = n$ consists of two leaves $\tilde{\mathcal{L}}_1^{(n)}$, two leaves $\hat{\mathcal{L}}_1^{(n)}$, and the core connecting the four leaves. All other leaves are substructures of these leaves, e.g., $\tilde{\mathcal{L}}_1^{(n)}$ consists of one leaf $\mathcal{L}_3^{(n)}$ and two leaves $\mathcal{L}_1^{(n)}$, where the leaves $\mathcal{L}_1^{(n)}$ are symmetrically equivalent. With this, denoting by $\tilde{S}(n)$, $S(n)$, and $S'(n)$ the number of distinct amplitudes in $\tilde{\mathcal{L}}_1^{(n)}$, $\mathcal{L}_1^{(n)}$, and $\mathcal{L}_3^{(n)}$, respectively, we get

$$\tilde{S}(n) = S(n) + S'(n). \quad (\text{A20})$$

where

$$\beta = \begin{cases} \mu_{134}^{(3)} & \text{for } (i, j) = (S(I), S(I)) \\ (\mathbf{A}^{(I)})_{ij} & \text{else,} \end{cases} \quad (\text{A29})$$

$$\gamma = \begin{cases} \mu_{134}^{(3)} & \text{for } (i, j) = (S'(I), S'(I)) \\ (\mathbf{H}^{(I)})_{ij} & \text{else,} \end{cases} \quad (\text{A30})$$

$$\mathbf{D}_{12} = \mathbf{D}_{21}^T = \begin{cases} \rho_3 & \text{for } (i, j) = (S'(I), S(I)) \\ 0 & \text{else,} \end{cases}$$

$$\mathbf{D}_{13} = \mathbf{D}_{31}^T = \begin{cases} v_{33} & \text{for } (i, j) = (S'(I), 1) \\ \rho_3 & \text{for } (i, j) \in \{(S'(I), 3), (S'(I) - 1, 1), \\ & (S'(I) - 2, 1)\} \\ 0 & \text{else,} \end{cases}$$

and

$$\mathbf{D}_{23} = \mathbf{D}_{32}^T = \begin{cases} v_{33} & \text{for } (i, j) = (S(I), 1) \\ \rho_3 & \text{for } (i, j) \in \{(S(I), 3), (S(I) - 1, 1), \\ & (S(I) - 2, 1)\} \\ 0 & \text{else.} \end{cases}$$

Now it is possible to construct the $\mathbf{A}^{(I+1)}$ related to the whole $\mathcal{L}_1^{(I+1)}$ leaf (see Fig. 12),

$$\mathbf{A}^{(I+1)} = \begin{pmatrix} \delta & \mathbf{E}_{12} & \mathbf{E}_{13} \\ \mathbf{E}_{21} & \epsilon & \mathbf{E}_{23} \\ \mathbf{E}_{31} & \mathbf{E}_{32} & \zeta \end{pmatrix}, \quad (\text{A31})$$

where

$$\delta = \begin{cases} \mu_{144}^{(3)} & \text{for } (i, j) = (\tilde{S}(I), \tilde{S}(I)) \\ (\tilde{\mathbf{A}}^{(I)})_{ij} & \text{else} \end{cases} \quad (\text{A32})$$

is related to $\tilde{\mathcal{L}}_1^{(I)}$ inside $\mathcal{L}_1^{(I+1)}$,

$$\epsilon = \begin{cases} \mu_{144}^{(3)} + \rho_4 & \text{for } (i, j) = (S(I), S(I)) \\ (\mathbf{A}^{(I)})_{ij} & \text{else} \end{cases} \quad (\text{A33})$$

to two cophasely moving symmetrically equivalent $\tilde{\mathcal{L}}_1^{(I)}$ inside $\mathcal{L}_1^{(I+1)}$, and

$$\zeta = \begin{cases} \mu_{134}^{(3)} - \rho_3 & \text{for } (i, j) = (2S'(I) + S(I), 2S'(I) + S(I)) \\ \mu_{333}^{(4)} & \text{for } (i, j) = (1, 1) \\ \mu_{144}^{(3)} & \text{for } (i, j) = (3, 3) \\ v_{34} & \text{for } (i, j) \in \{(3, 1), (1, 3)\} \\ (\tilde{\mathbf{H}}^{(I)})_{ij} & \text{else} \end{cases} \quad (\text{A34})$$

to the leaves $\mathcal{L}_4^{(I)}$, $\mathcal{L}_3^{(I)}$, and $\mathcal{L}_1^{(I)}$ inside $\mathcal{L}_1^{(I+1)}$. The connection blocks are

$$\mathbf{E}_{12} = 2\mathbf{E}_{21}^T = \begin{cases} 2\rho_4 & \text{for } (i, j) = (\tilde{S}(I), S(I)) \\ 0 & \text{else,} \end{cases}$$

$$\mathbf{E}_{13} = \mathbf{E}_{31}^T = \begin{cases} v_{34} & \text{for } (i, j) = (\tilde{S}(I), 1) \\ \rho_4 & \text{for } (i, j) = (\tilde{S}(I), 3) \\ \rho_3 & \text{for } (i, j) \in \{(\tilde{S}(I) - 1, 1), \\ & (\tilde{S}(I) - 2, 1)\} \\ 0 & \text{else,} \end{cases}$$

and

$$2\mathbf{E}_{23} = \mathbf{E}_{32}^T = \begin{cases} 2v_{34} & \text{for } (i, j) = (S(I), 1) \\ 2\rho_4 & \text{for } (i, j) = (S(I), 3) \\ 2\rho_3 & \text{for } (i, j) \in \{(S(I) - 1, 1), \\ & (S(I) - 2, 1)\} \\ 0 & \text{else.} \end{cases}$$

The auxiliary matrix $\mathbf{H}^{(I+1)}$ can be constructed from already-known parts. One gets

$$\mathbf{H}^{(I+1)} = \begin{cases} \mu_{144}^{(3)} - \rho_4 & \text{for } (i, j) = (S'(I + 1), \\ & S'(I + 1)) \\ \mu_{333}^{(3)} & \text{for } (i, j) = (1, 1) \\ \mu_{134}^{(3)} & \text{for } (i, j) = (3, 3) \\ v_{33} & \text{for } (i, j) \in \{(1, 3), (3, 1)\} \\ (\mathbf{H}_1^{(I+1)})_{ij} & \text{else,} \end{cases} \quad (\text{A35})$$

where

$$\mathbf{H}_1^{(I+1)} = \begin{pmatrix} \eta & \mathbf{F}_{12} & \mathbf{F}_{13} \\ \mathbf{F}_{21} & \epsilon & \mathbf{F}_{23} \\ \mathbf{F}_{31} & \mathbf{F}_{32} & \eta \end{pmatrix} \quad (\text{A36})$$

with

$$\eta = \begin{cases} \mu_{144}^{(3)} & \text{for } (i, j) = (2S'(I) + S(I), 2S'(I) + S(I)) \\ (\zeta)_{ij} & \text{else} \end{cases} \quad (\text{A37})$$

and

$$\mathbf{F}_{12} = 2\mathbf{F}_{21}^T = \begin{cases} 2\rho_4 & \text{for } (i, j) = (2S'(I) + S(I), S(I)) \\ 0 & \text{else,} \end{cases}$$

$$\mathbf{F}_{13} = \mathbf{F}_{31}^T = \begin{cases} v_{34} & \text{for } (i, j) = (2S'(I) + S(I), 1) \\ \rho_4 & \text{for } (i, j) = (2S'(I) + S(I), 3) \\ \rho_3 & \text{for } (i, j) \in \{(2S'(I) + S(I) - 1, 1), \\ & (2S'(I) + S(I) - 2, 1)\} \\ 0 & \text{else,} \end{cases}$$

$$2\mathbf{F}_{23} = \mathbf{F}_{32}^T = \begin{cases} 2v_{34} & \text{for } (i, j) = (S(I), 1) \\ 2\rho_4 & \text{for } (i, j) = (S(I), 3) \\ 2\rho_3 & \text{for } (i, j) \in \{(S(I) - 1, 1), \\ & (S(I) - 2, 1)\} \\ 0 & \text{else.} \end{cases}$$

f. Construction of $\mathbf{B}^{(I)}$

The reduced matrices related to the modes in which the core of the tree is mobile read

$$\mathbf{B}^{(I)} = \begin{pmatrix} \boldsymbol{\theta} & \mathbf{I}_{12} & \mathbf{I}_{13} \\ \mathbf{I}_{21} & \boldsymbol{\epsilon} & \mathbf{I}_{23} \\ \mathbf{I}_{31} & \mathbf{I}_{32} & \mu_{3333}^{(4)} \end{pmatrix}, \quad (\text{A38})$$

$$\boldsymbol{\theta} = \begin{cases} \mu_{144}^{(3)} + \rho_4 & \text{for } (i, j) = (\tilde{S}(I), \tilde{S}(I)) \\ (\tilde{\mathbf{A}}^{(I)})_{ij} & \text{else,} \end{cases} \quad (\text{A39})$$

$$\mathbf{I}_{12} = \mathbf{I}_{21}^T = \begin{cases} 2\rho_4 & \text{for } (i, j) = (\tilde{S}(I), S(I)) \\ 0 & \text{else,} \end{cases}$$

$$2\mathbf{I}_{13} = \mathbf{I}_{31}^T = \begin{cases} 2\nu_{34} & \text{for } (i, j) = (\tilde{S}(I), 1) \\ 2\rho_3 & \text{for } (i, j) \in \{(\tilde{S}(I) - 1, 1), \\ & (\tilde{S}(I) - 2, 1)\} \\ 0 & \text{else,} \end{cases}$$

$$2\mathbf{I}_{23} = \mathbf{I}_{32}^T = \begin{cases} 2\nu_{34} & \text{for } (i, j) = (S(I), 1) \\ 2\rho_3 & \text{for } (i, j) \in \{(S(I) - 1, 1), \\ & (S(I) - 2, 1)\} \\ 0 & \text{else.} \end{cases}$$

-
- [1] B. B. Mandelbrot, *The Fractal Geometry of Nature* (W.H. Freeman & Co., New York, CA, 1982).
- [2] T. R. Nelson, B. J. West, and A. L. Goldberger, *Cell. Mol. Life Sci.* **46**, 251 (1990).
- [3] E. R. Weibel, *Am. J. Physiol.* **261**, L361 (1991).
- [4] F. E. Lennon *et al.*, *Nat. Rev. Clin. Oncol.* **12**, 664 (2015).
- [5] P. Turner and L. Nottale, *Progr. Biophys. Mol. Biol.* **123**, 48 (2017).
- [6] S. Reuveni, R. Granek, and J. Klafter, *Phys. Rev. Lett.* **100**, 208101 (2008).
- [7] S. Reuveni, R. Granek, and J. Klafter, *Proc. Natl. Acad. Sci. USA* **107**, 13696 (2010).
- [8] E. Lieberman-Aiden *et al.*, *Science* **326**, 289 (2009).
- [9] L. A. Mirny, *Chromosome Res.* **19**, 37 (2011).
- [10] G. Fudenberg, G. Getz, M. Meyerson, and L. A. Mirny, *Nat. Biotechnol.* **29**, 1109 (2011).
- [11] A. Y. Grosberg, *Polym Sci. Ser. C* **54**, 1 (2012).
- [12] L. M. Almossalha *et al.*, *Sci. Rep.* **7**, 41061 (2017).
- [13] S. Shibuichi, T. Onda, N. Satoh, and K. Tsujii, *J. Phys. Chem.* **100**, 19512 (1996).
- [14] K. Tsujii, *Polym. J.* **40**, 785 (2008).
- [15] Q. Zeng, M. Luo, X. Pang, L. Li, and K. Li, *Appl. Surf. Sci.* **282**, 302 (2013).
- [16] H.-X. Xu, G.-M. Wang, M. Q. Qi, L. Li, and T. J. Cui, *Adv. Opt. Mat.* **1**, 495 (2013).
- [17] Y. Zhang, Y. Huang, and J. A. Rogers, *Curr. Op. Sol. State Mater. Sci.* **19**, 190 (2015).
- [18] J. Ge, G. Fan, Y. Si, J. He, H.-Y. Kim, B. Ding, S. S. Al-Deyab, M. El-Newehy, and J. Yu, *Nanoscale* **8**, 2195 (2016).
- [19] S. K. Nechaev and K. Polovnikov, *Soft Matter* **13**, 1420 (2017).
- [20] M. Dolgushev, J. P. Wittmer, A. Johner, O. Benzerara, H. Meyer, and J. Baschnagel, *Soft Matter* **13**, 2499 (2017).
- [21] M. Müller, J. P. Wittmer, and M. E. Cates, *Phys. Rev. E* **53**, 5063 (1996).
- [22] M. Müller, J. P. Wittmer, and M. E. Cates, *Phys. Rev. E* **61**, 4078 (2000).
- [23] J. D. Halverson, W. B. Lee, G. S. Grest, A. Y. Grosberg, and K. Kremer, *J. Chem. Phys.* **134**, 204904 (2011).
- [24] J. D. Halverson, W. B. Lee, G. S. Grest, A. Y. Grosberg, and K. Kremer, *J. Chem. Phys.* **134**, 204905 (2011).
- [25] S. Obukhov, A. Johner, J. Baschnagel, H. Meyer, and J. P. Wittmer, *Europhys. Lett.* **105**, 48005 (2014).
- [26] A. Y. Grosberg, *Soft Matter* **10**, 560 (2014).
- [27] T. Sakaue, *Phys. Rev. Lett.* **106**, 167802 (2011).
- [28] A. Rosa and R. Everaers, *Phys. Rev. Lett.* **112**, 118302 (2014).
- [29] D. Michieletto and M. S. Turner, *Proc. Natl. Acad. Sci. USA* **113**, 5195 (2016).
- [30] T. Ge, S. Panyukov, and M. Rubinstein, *Macromolecules* **49**, 708 (2016).
- [31] J. Smrek and A. Y. Grosberg, *ACS Macro Lett.* **5**, 750 (2016).
- [32] M. Kapnistos, M. Lang, D. Vlassopoulos, W. Pyckhout-Hintzen, D. Richter, D. Cho, T. Chang, and M. Rubinstein, *Nat. Mater.* **7**, 997 (2008).
- [33] S. Goossen, A. R. Brás, M. Krutyeva, M. Sharp, P. Falus, A. Feoktystov, U. Gasser, W. Pyckhout-Hintzen, A. Wischniewski, and D. Richter, *Phys. Rev. Lett.* **113**, 168302 (2014).
- [34] P. Polińska, C. Gillig, J. P. Wittmer, and J. Baschnagel, *Eur. Phys. J. E* **37**, 12 (2014).
- [35] A. A. Gurtovenko and A. Blumen, *Adv. Polym. Sci.* **182**, 171 (2005).
- [36] M. Doi and S. F. Edwards, *The Theory of Polymer Dynamics* (Clarendon Press, London, 1988).
- [37] We note that in the framework used here (which stems from Ref. [38] for linear chains) the length of each bond is not constant (unlike for the classical freely rotating chain model). Each bond can fluctuate with the fixed mean-square length b^2 . This assumption allows to describe polymers by a (multivariate) Gaussian distribution.
- [38] M. Bixon and R. Zwanzig, *J. Chem. Phys.* **68**, 1896 (1978).
- [39] M. Dolgushev and A. Blumen, *J. Chem. Phys.* **131**, 044905 (2009).
- [40] F. Fürstenberg, M. Dolgushev, and A. Blumen, *J. Chem. Phys.* **136**, 154904 (2012).
- [41] J. Grimm and M. Dolgushev, *Phys. Chem. Chem. Phys.* **18**, 19050 (2016).
- [42] F. Fürstenberg, M. Dolgushev, and A. Blumen, *J. Chem. Phys.* **138**, 034904 (2013).
- [43] J. Mielke and M. Dolgushev, *Polymers* **8**, 263 (2016).
- [44] A. Kumar and P. Biswas, *Phys. Chem. Chem. Phys.* **15**, 20294 (2013).
- [45] D. A. Markelov, S. G. Falkovich, I. M. Neelov, M. Y. Ilyash, V. V. Matveev, E. Lähderanta, P. Ingman, and A. A. Darinskii, *Phys. Chem. Chem. Phys.* **17**, 3214 (2015).
- [46] D. A. Markelov, A. N. Shishkin, V. V. Matveev, A. V. Penkova, E. Lähderanta, and V. I. Chizhik, *Macromolecules* **49**, 9247 (2016).

- [47] O. V. Shavykin, I. M. Neelov, and A. A. Darinskii, *Phys. Chem. Chem. Phys.* **18**, 24307 (2016).
- [48] M. L. Mansfield and W. H. Stockmayer, *Macromolecules* **13**, 1713 (1980).
- [49] The eigenvectors of the set are linearly independent, but not necessarily orthogonal.
- [50] C. Cai and Z. Y. Chen, *Macromolecules* **30**, 5104 (1997).
- [51] M. Dolgushev, G. Berezovska, and A. Blumen, *J. Chem. Phys.* **133**, 154905 (2010).
- [52] S. Alexander and R. Orbach, *J. Phys. Lett.* **43**, 625 (1982).
- [53] W. C. Forsman, *J. Chem. Phys.* **65**, 4111 (1976).
- [54] B. E. Eichinger, *Macromolecules* **13**, 1 (1980).
- [55] A. Jurjiu, R. Dockhorn, O. Mironova, and J.-U. Sommer, *Soft Matter* **10**, 4935 (2014).
- [56] K.-h. Nitta, *J. Chem. Phys.* **101**, 4222 (1994).
- [57] The exponent $1/3$ is related to the spectral dimension $d_s = 6/5$ by $(2 - d_s)/2d_s = 1/3$, see, e.g., Ref. [55].
- [58] We note that in simulations one usually calculates preaveraged asphericity and prolateness, i.e., based on the average $\{\langle\sigma_i\rangle\}$ and $\langle R_g^2\rangle$.
- [59] J. Rudnick and G. Gaspari, *J. Phys. A: Math. Gen.* **19**, L191 (1986).
- [60] J. Rudnick and G. Gaspari, *Science* **237**, 384 (1987).
- [61] G. Wei, *Physica A* **222**, 152 (1995).
- [62] G. Wei, *Macromolecules* **30**, 2125 (1997).
- [63] G. Wei, *Macromolecules* **30**, 2130 (1997).
- [64] G. Zifferer, *J. Chem. Phys.* **110**, 4668 (1999).
- [65] C. von Ferber, J. Y. Monteith, and M. Bishop, *Macromolecules* **42**, 3627 (2009).
- [66] C. von Ferber, M. Bishop, T. Forzaglia, C. Reid, and G. Zajac, *J. Chem. Phys.* **142**, 024901 (2015).
- [67] O. Kalyuzhnyi, J. M. Ilnytskyi, Y. Holovatch, and C. von Ferber, *J. Phys.: Cond. Mat.* **28**, 505101 (2016).
- [68] D. J. Klein and M. Randić, *J. Math. Chem.* **12**, 81 (1993).
- [69] F. Fouss, A. Pirotte, J.-M. Renders, and M. Saerens, *IEEE Trans. Knowl. Data Eng.* **19**, 355 (2007).
- [70] Z. Zhang, B. Wu, H. Zhang, S. Zhou, J. Guan, and Z. Wang, *Phys. Rev. E* **81**, 031118 (2010).
- [71] J. P. Wittmer, I. Kriuchevskiy, A. Cavallo, H. Xu, and J. Baschnagel, *Phys. Rev. E* **93**, 062611 (2016).